A capacitive vibration-to-electricity energy converter with integrated mechanical switches

2008 J. Micromech. Microeng. 18 104004

(http://iopscience.iop.org/0960-1317/18/10/104004)

J. Micromech. Microeng. **18** (2008) 104004 (8pp) doi:10.1088/0960-1317/18/10/104004

A capacitive vibration-to-electricity energy converter with integrated mechanical switches

Y Chiu and V F G Tseng

Department of Electrical and Control Engineering, National Chiao Tung University, Hsinchu, 300, Taiwan, Republic of China

E-mail: yichiu@mail.nctu.edu.tw

Received 7 April 2008, in final form 17 June 2008
Published 29 September 2008
Online at stacks.iop.org/JMM/18/104004

Abstract

Due to recent advances in low-power VLSI design technology, it has become feasible to power portable or remote electronic devices by scavenging the ambient energy. The design, fabrication and measurement of a capacitive vibration-to-electricity energy converter are presented in this paper. With a device area constraint of 1 cm^2 and an auxiliary battery supply of 3.6 V, the device was designed to generate an output power of 31 μW with an output saturation voltage of 40 V. An external mass of 4 g was needed to adjust the device resonance to match the input vibration of 2.25 m s^{-2} at 120 Hz. Mechanical contact switches were integrated onto the device to provide accurate charge–discharge energy conversion timing. The device was fabricated in SOI (silicon-on-insulator) wafers by deep silicon etching technology. Parasitic capacitance was minimized by partial back side substrate removal. Resonant frequencies of the fabricated device with and without the external mass agreed with the expected values. Without the external mass, the measured ac output power was 1.2 μW with a load of 5 MΩ at 1870 Hz. Detailed circuit modeling and ac output power measurement of the devices with the external mass attached are in progress.

1. Introduction

The continuous improvement of microsystem technology promotes the development of smart micro transducer networks, such as RFID (radio frequency identification), wireless sensor networks [1] and personal health monitoring [2]. These highly integrated sensor modules have received increasing interest in recent years. Nevertheless, power consumption has become a severe constraint on their development and application due to the limited capacity of small energy storage devices, such as batteries and, as a more recent development, ultra capacitors [3]. Microfabricated or miniaturized energy storage or supply devices are also under intensive study, including micro batteries [4], micro fuel cells [5], micro heat engines [6], radioactive materials [7] and so forth. While researchers are trying to increase the energy density in these storage devices, the solutions still have finite lifetime and therefore high maintenance costs.

Fortunately, the advance in low-power VLSI (very large scale integrated circuit) technology, along with the low duty cycles of wireless sensor networks, has reduced power requirements of the sensor modules to tens to hundreds of microwatts [8]. It then becomes possible to power these devices by scavenging ambient energy from the environment, thus providing a self-renewable or sustainable energy source. Energy scavenging devices can extract energy from a wide range of ambient energy sources, such as light exposure [9, 10], thermal gradients [11–13], human kinetic power [14, 15], air flow [16, 17] and acoustic noise [18]. Similar but unlike human or acoustic vibration, the ambient vibration is another widely available energy source. It can be observed in large commercial and office buildings, factories, automobiles, aircrafts, ships, trains, industrial machinery and household appliances. Different conversion technologies are utilized for different types of vibration sources. Theory and experiments show that more than 300 μW cm^{-3} can be generated [19]. The potential of this method is greatly amplified when targeted on specific vibration sources.

Typical vibration-to-electricity energy conversion technology is based on three mechanisms, namely

electromagnetic inductive conversion [8, 20–23], electrostatic capacitive conversion [24–28] and piezoelectric conversion [29–32]. Electromagnetic energy conversion is based on Faraday's law of induction. The most common drawback of microelectromagnetic energy conversion is the relatively low induced voltage, which can be foreseen from the scaling law of the electromagnetic effect. Difficulty in fabricating high quality coils with a large number of turns in thin film processes is also a major challenge. Piezoelectric energy conversion relies on the piezoelectric effect of specific materials in the presence of an applied mechanical strain. However, materials with high piezoelectric constants, such as PZT, are not compatible with conventional IC processes. Electrostatic capacitive energy conversion utilizes a variable capacitor to convert the vibration energy into electric energy. MEMS variable capacitors can be fabricated through a mature silicon-based micromachining process. Therefore, the capacitive energy conversion is the most compatible approach with IC processes. Although an external voltage source V_{in} may be needed to charge the variable capacitor, it can also be charged by an electret [33, 34], by a built-in voltage due to work function difference [35], or by employing a self-recharge circuitry [26] to extend the lifetime of the voltage source.

The extraction of the energy in capacitive energy conversion must be accurately synchronized to the vibration in order to achieve high conversion efficiency. A prototype circuitry was proposed in [19] in which the timing switches were replaced by diodes. However, this model results in an excessive output power reduction due to the far-from-ideal characteristics of the diodes. Other researches [25, 26, 36, 37] utilized gate-clocked MOSFET switches or other circuit configuration. However, power consumption and parasitics of the electronics can still degrade the performance of the converters. Since the operation of the converter depends on the mechanical oscillation of a proof mass, mechanical contact switches that turn on or off according to the position of the proof mass can work synchronously in the converter. Such switches were employed in a non-resonant converter [24]. As opposed to our previous work where the switches were modeled as ideal diodes [27], novel integrated mechanical switches are proposed for a resonant electrostatic vibration-to-electricity energy converter in this paper. Compared to traditional design with diodes or active electric circuit components, the mechanical switches have the advantage of zero leakage current, low power consumption and synchronous operation. The design, fabrication and preliminary measurement results are presented.

2. Device design

The targeted vibration source in our design is 2.5 m s^{-2} at 120 Hz measured on a typical household air conditioner [27]. The converter is composed of a 3.6 V auxiliary battery supply V_{in} (such as a Li-ion rechargeable battery), a vibration-driven variable capacitor C_v and an output storage capacitor C_{stor} connected with the load R_L, as shown in figure 1. A basic operation cycle begins when the variable capacitor C_v is

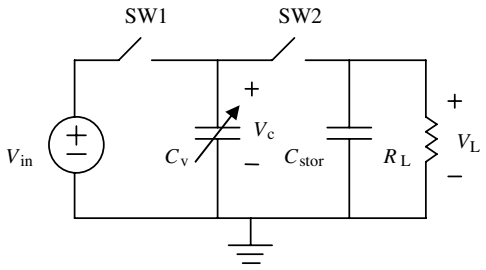

Figure 1. Schematic of the electrostatic energy converter.

charged by V_{in} through SW1 at its maximum C_{max}. After C_v is charged to V_{in}, SW1 is opened and the capacitance changes from C_{max} to C_{min} due to vibration-driven displacement. In this process, the charge Q on the capacitor remains constant (SW1 and SW2 both open). Therefore, the terminal voltage on the capacitor is increased, converting the kinetic energy of vibration into electrical energy stored in C_v. When the capacitance reaches C_{min} and terminal voltage reaches V_{max}, SW2 closes and allows C_{stor} to be charged by C_v through charge redistribution, transferring the energy to the output port. SW2 is then opened and C_v changes back to C_{max}, preparing for the next conversion cycle. During this period, the charge on C_{stor} is dissipated through the load resistance R_L. To achieve high conversion efficiency, the charge–discharge cycles and the operations of the switches must be timed precisely with the variation of the capacitance.

2.1. Variable capacitance

For perfectly synchronized switch operation, it was shown in [27] that the steady-state saturation output voltage can be approximated as

$$V_{sat} \approx \frac{C_{max} R_L V_{in}}{\Delta t} \tag{1}$$

if $R_L C_{min} \ll \Delta t \ll R_L C_{stor}$, where $\Delta t = 1/2f$ is the conversion cycle time and f is the vibration frequency. The output power becomes

$$P_{out} \approx \frac{V_{sat}^2}{R_L} \approx \left(\frac{C_{max} V_{in}}{\Delta t}\right)^2 R_L. \tag{2}$$

The MEMS variable capacitor C_v is formed by an in-plane gap-closing comb structure [28], as shown in figure 2(*a*). From the required output voltage and power, C_{min}, C_{max}, C_{stor} and R_L can be determined from the above static analysis. Since the values of C_{min} and C_{max} depend on the geometry and material used to fabricate the device, the layout and process flow can be designed according to the processing capability. The spring constant of the suspension and the proof mass can then be adjusted to match the resonant frequency so that the required displacement of the proof mass can be achieved for C_{min} and C_{max} as expected in the above static analysis. However, the constant charge Q in the variable capacitor results in an electrostatic force that behaves like a negative spring. Since Q changes constantly in the charge–discharge cycles, the electrostatic spring has a time-varying nature. It inevitably interferes with the oscillation dynamics. Therefore,

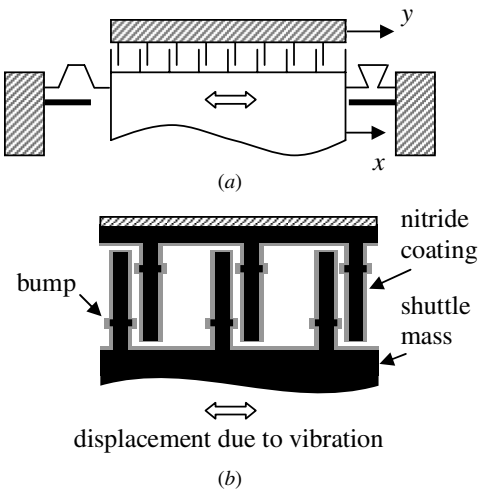

Figure 2. (*a*) In-plane gap-closing variable capacitor and (*b*) bumps on comb fingers.

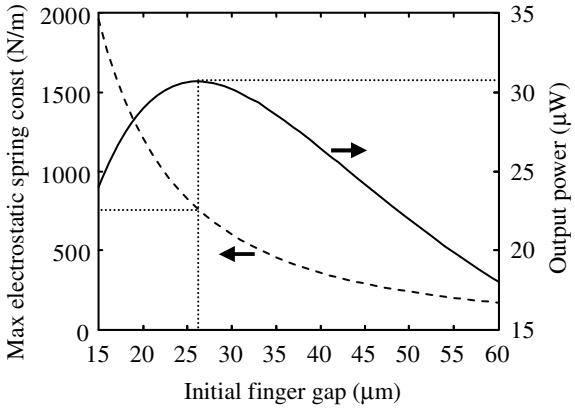

Figure 3. Output power and maximum b_e versus the initial finger gap.

the above design flow must be iterated between static and dynamic analyses until a smooth mechanical oscillation can be maintained.

The maximum value of C_v (C_{max}) can be increased by reducing the minimum gap spacing. In our design, silicon nitride ($\varepsilon_r = 7$) is deposited on finger sidewalls to prevent shortage between fingers. It also increases C_{max} without significantly increasing C_{min}. The comb fingers are designed with 'bumps' on the sidewalls for a more compliant minimum air gap control even in the presence of etching tolerance and finger contact, as shown in figure 2(*b*). The minimum air gap of 0.5 μm, sidewall silicon nitride thickness of 500 Å, finger thickness (height) of 200 μm and finger width of 10 μm are predetermined in consideration of the control of thin film thickness and the aspect ratio in deep silicon etching. The output voltage is limited to 40 V to be compatible with high-voltage power management circuits. For a device area of 1 cm^2, and V_{in} of 3.6 V, figure 3 shows the output power and maximum electrostatic spring constant b_e as a function of the initial finger gap distance. Therefore, an output power of 31 μW can be achieved with an initial finger gap of 26 μm, and the corresponding value of b_{e_max} is 774 μN μm^{-1}. The other

Table 1. Variable capacitor design and performance parameters.

Description of variables	Value
Finger thickness (height)	200 μm
Number of variable capacitor cells	1126
Finger width	10 μm
Finger length	425 μm
Finger overlap	400 μm
Initial finger gap	26 μm
Minimum air gap	0.5 μm
Sidewall silicon nitride thickness	500 Å
Maximum value of capacitance C_{max}	1570 pF
Minimum value of capacitance C_{min}	62 pF
Maximum electrostatic spring const b_{e_max}	774 μN μm^{-1}
Load resistance R_L	50 MΩ
Output storage capacitor C_{stor}	5 nF
Voltage ripple	<1 V
Output voltage (steady state) V_{out}	40 V
Output power (steady state) P_{out}	31 μW

design and performance parameters of the variable capacitor are listed in table 1, which contains optimized results from the iteration between static and dynamic designs. Some of the tradeoff between the static and dynamic characteristics is discussed in the next section.

2.2. Dynamic simulation

The electro-mechanical dynamics of the variable capacitor can be modeled as a spring–damper-mass system [19, 27],

$$m\ddot{x} + b_m(x)\dot{x} + kx + b_e x = -m\ddot{y}, \tag{3}$$

where y is the displacement of the device frame caused by the ambient vibration, x is the relative displacement between movable and fixed electrodes, $b_m(x)\dot{x}$ is the nonlinear mechanical damping force caused by the squeezed film effect, kx is the mechanical spring force and $b_e x$ is the electrostatic force caused by the charge on the capacitor. The electrostatic force acts as a negative spring force to soften the mechanical spring. The total spring constant of the system becomes $k_{total} = k + b_e < k$. Therefore b_e should be as low as possible in order not to disrupt the mechanical oscillation by the electrostatic pull-in effect. Furthermore, the charge or discharge of the variable capacitor causes an abrupt change of Q and results in an electrostatic impact force on the proof mass to disturb its oscillation. The electrostatic force and b_e are determined by the maximum value of Q on the capacitor $Q_{max} = C_{max} V_{in}$. Therefore, C_{max} should be limited to limit the electrostatic effect on the mechanical oscillation. This is the most important tradeoff in designing the electrostatic energy converter since reduced C_{max} implies reduced output power.

Simulink was used to simulate the dynamic behavior of the system in the presence of the nonlinear damping force b_m and time-varying electrostatic force b_e. Figure 4 gives a summary of the simulation and shows the minimum k/b_{e_max} ratio to maintain a steady oscillation with the desired maximum displacement. For a maximum displacement of 26 μm, the spring constant k and the proof mass m can be calculated as 2425 μN μm^{-1} and 4 g, respectively, from figures 3 and 4. The simulated time response of the output voltage is shown in

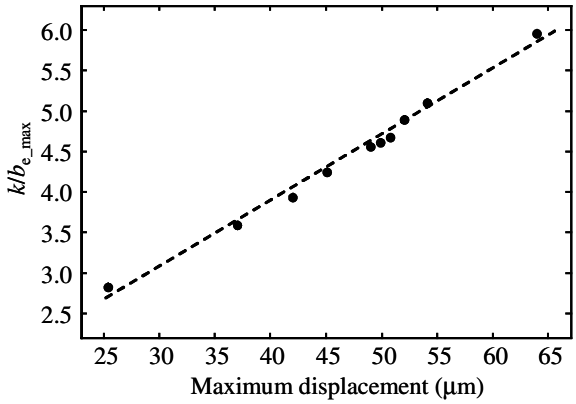

Figure 4. k/b_{e_max} ratio versus oscillation amplitude.

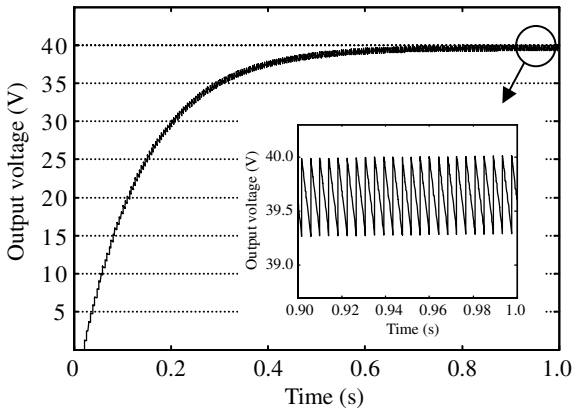

Figure 5. Simulated time response of the output voltage.

figure 5. The saturation voltage is close to the expected 40 V. This is equivalent to 31 μW power delivered to a load of 50 MΩ. The closeup view of the steady-state response shows an output voltage ripple below 1 V.

2.3. Mechanical switches

The switches SW1 and SW2 are realized as lateral contact mechanical switches. They have barely zero charge leakage and a very low capacitive coupling effect. Other advantages include low energy consumption, synchronous operation to the variable capacitor and monolithic integration with the whole device structure.

2.3.1. SW1 design. SW1 should ideally be closed when the movable electrode of the variable capacitor is near the maximum displacement, and opened immediately after charging is finished. In our design, one end (N2) of SW1 is attached to the movable electrode of C_v and the other (N1) to the charging terminal, as shown in figure 6. SW1 laterally contacts at the maximum displacement (C_{max}) position. A more compliant contact mechanism is designed with a spring structure to provide a 1.16 mN restoring force at an extra displacement of 1 μm for low contact resistance during charging.

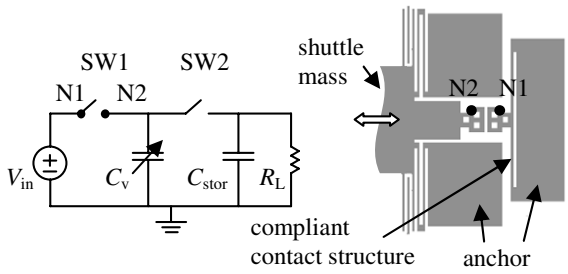

Figure 6. Mechanical switch SW1: schematic and layout.

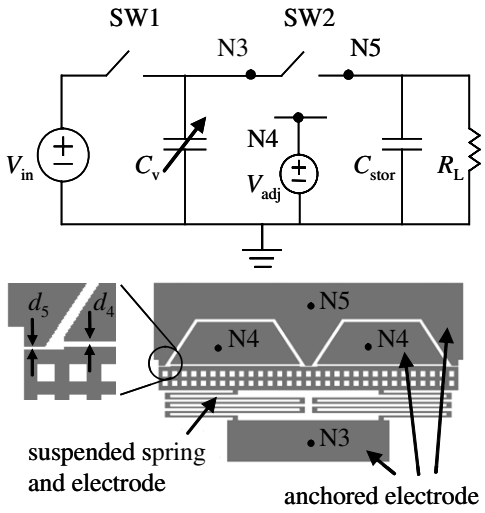

Figure 7. Mechanical switch SW2: schematic and layout.

2.3.2. SW2 design. SW2 should ideally be closed when the variable capacitor moves to the center position. At this position, the terminal voltage of C_v has a maximum value V_{max}. As shown in figure 7, this high voltage at node N3 is used to induce electrostatic pull-in between N3 and N4, which is normally connected to ground. The gap between N3 and N5 (d_5) is smaller than that between N3 and N4 (d_4). Therefore, N3 will contact the output port N5 to close the switch before it is shorted to N4. N4 can also be connected to an adjustment voltage V_{adj} to tune the pull-in timing of the switch to match the dynamics of the variable capacitor under fabrication uncertainties and device parasitics.

The pull-in voltage of gap d_4 can be determined by the following equation [38]:

$$V_{PI} = \sqrt{\frac{8}{27}\frac{k_{SW2}d_4^3}{\varepsilon h L_{SW2}}}, \tag{4}$$

where k_{SW2} is the suspension spring constant, and L_{SW2} is the total overlap length of nodes N3 and N4. The thickness h is identical to that of the variable capacitor. The maximum voltage V_{max} of the variable capacitor on N3 is

$$V_{max} = \frac{C_{max} + C_p}{C_{min} + C_p} V_{in} > \frac{C_{max}}{C_{min}} V_{in} \approx 90\ \text{V}, \tag{5}$$

where C_p is the parasitic capacitance due to substrates and anchors. Therefore, the pull-in voltage should be designed to be lower than 90 V. Once C_p is determined by measurement

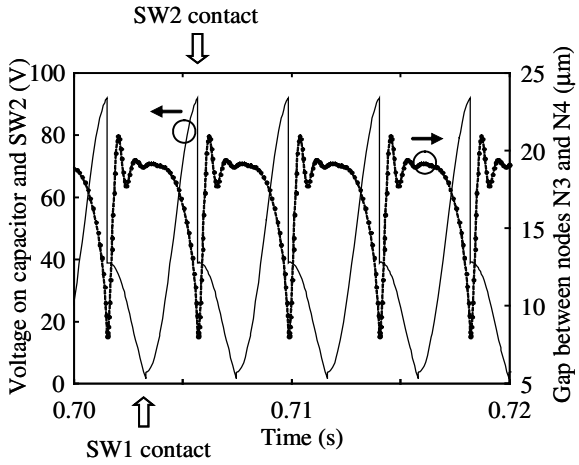

Figure 8. Time response of V_c and gap spacing in SW2.

or simulation, V_{adj} can be tuned so that $V_{PI} \leqslant V_{max} - V_{adj}$ to ensure the proper timing of SW2. When the charge on C_v is transferred to C_{stor} and the voltage between N3 and N4 drops below the release voltage V_R, SW2 will release and open. The release voltage is determined by [38]

$$V_R = \sqrt{\frac{2k_{SW2}d_5(d_4 - d_5)^2}{\varepsilon h L_{SW2}}}. \quad (6)$$

V_R should be designed to be higher than the output saturation voltage V_{sat}, which is about 40 V in the current design. If V_{sat} is affected by the parasitic capacitance, V_{adj} can also be used to tune the release operation of the switch. SW2 is designed in accordance with the above specifications. Figure 8 shows the simulated voltage V_c on node N3 and the gap spacing of SW2 in steady oscillation. It can been seen that as V_c approaches V_{PI}, the gap distance is rapidly reduced due to the pull-in effect. Upon the contact of SW2, V_c is dropped due to the charge transfer to C_{stor}. When SW2 is released, its position undergoes an underdamped ringing before settling down to the initial position. The charging by V_{in} upon the contact of SW1 can also be seen in the figure.

3. Device fabrication

The device was fabricated in a silicon-on-insulator (SOI) wafer with a 200 μm thick low-resistance (0.01–0.02 Ω cm) device layer. The device structure was first defined by inductively-coupled-plasma (ICP) etching on the front side. The back side was then deep etched to remove the substrate under the fingers to reduce parasitic capacitance. Care must be taken in the layout design to include block and guarding structures to define the etched patterns [39]. This can reduce the problem with different etching rates for different-sized openings. It also helps prevent the delicate structures in the device layer from being destroyed by the residual stress in the exposed buried oxide. After the deep silicon etching, the device was released in buffered HF solution. Silicon nitride was then deposited by plasma-enhanced chemical vapor deposition (PECVD) to cover the top surface and finger sidewalls. Metallization for the electrical bonding pad and lateral contact switches was

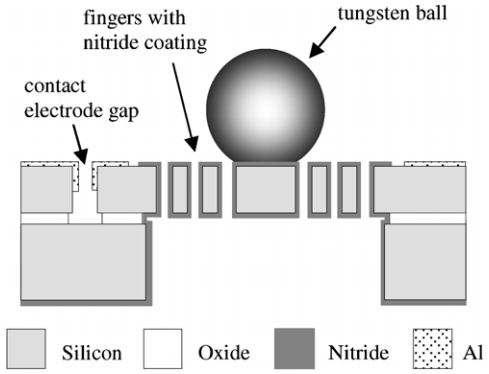

Figure 9. Cross section view of the fabricated device.

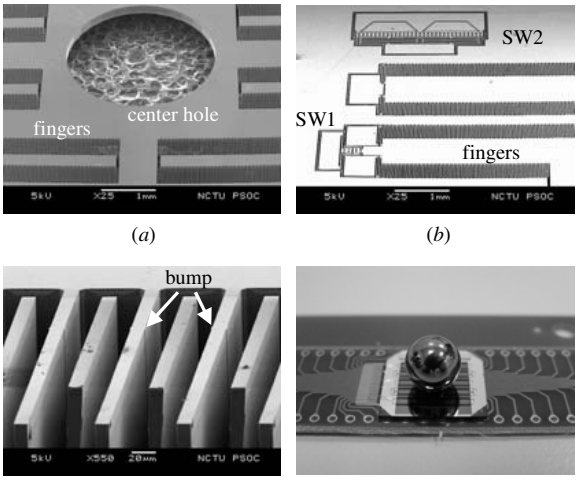

Figure 10. Fabricated device: (*a*) center hole for positioning the external mass, (*b*) SW1 and SW2, (*c*) fingers with bumps on the sidewall and (*d*) external mass attached for testing.

accomplished by first removing the top nitride with reactive ion etching (RIE) and then depositing metal by sputtering or evaporation, both through shadow masks. The device was then wire bonded and the external tungsten ball was attached for testing. Figure 9 shows the schematic cross section view of the device with the external mass attached. Figure 10 shows the SEM and optical micrographs of the fabricated device.

4. Measurement and discussion

After the device was fabricated, a 4 g (ϕ 4 mm) tungsten ball as the external mass was carefully placed in the center hole (figure 10(*a*)) and bonded to the device. The relative displacement of the movable part with respect to the device frame was measured with a MEMS motion analyzer (MMA). Without the external mass, the resonant frequency was 1870 Hz, in agreement with the expected value after correction for the change of spring width in the deep Si etch. Figure 11 shows the measured response with the external mass attached, showing a typical base-driven oscillation with the resonant frequency around the expected 120 Hz. The minor difference is caused by the error in the external mass and the spring

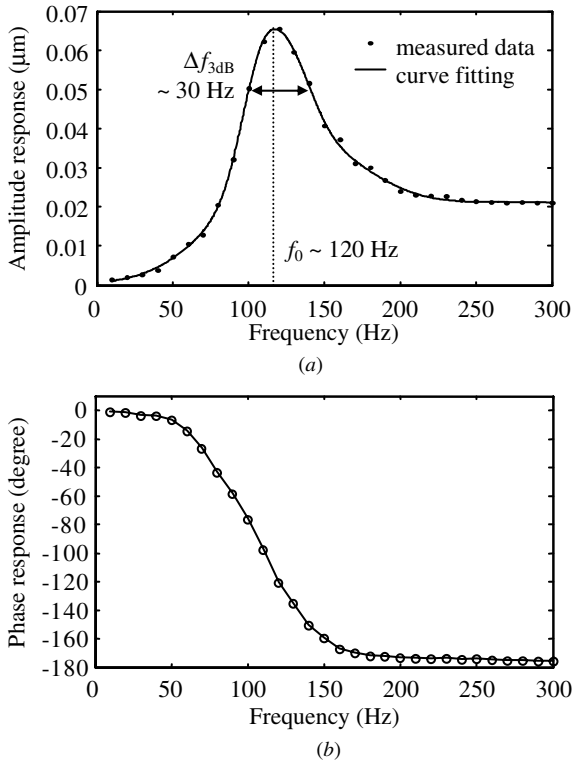

Figure 11. MMA measurement of a device with the external mass: (*a*) amplitude response and (*b*) phase response.

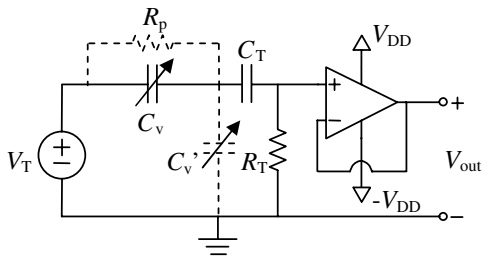

Figure 12. AC mode operation and measurement.

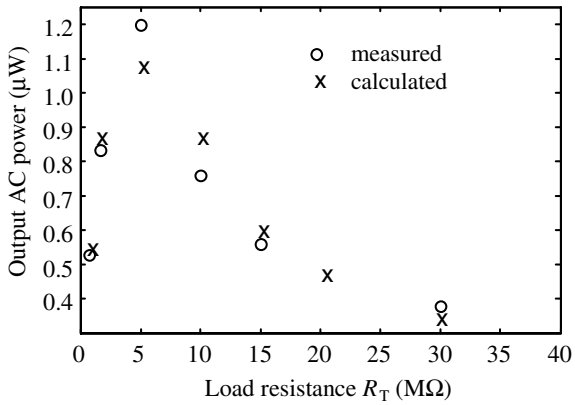

Figure 13. Measured and calculated ac output power versus load resistance.

width. However, the resonance has a quality factor of about 4, which is low compared with conventional MEMS resonating devices. This is possibly due to two reasons. First, the number of finger gaps is extremely large in this device and therefore results in large squeeze film damping. This effect can be solved in principle if the device is packaged in a low-pressure environment. Second, residual particles or depositions can be stuck in the finger gaps in the long, deep and narrow comb structure of the variable capacitor. This introduces additional mechanical damping. The mask layout design and processing parameters are currently being reviewed to eliminate this effect.

The impedance of the variable capacitor was measured with an INSTEK-LCR-816 LCR meter. A micro probe was used to displace the fingers and measurements were taken at various gap spacings. The measured minimum capacitance at zero displacement was about 120 pF, indicating a parasitic capacitance of about 60 pF in the device caused by anchors and substrate. The maximum capacitance at maximum displacement was only about 300 pF, indicating an effective displacement of only about 22 μm. This reduced maximum capacitance has a great effect on the output power. It is caused by the tolerance of the deep RIE process where (1) the overall dimensional variation of the etched patterns can change the relative positions of the movable parts and the fixed mechanical stops and thus change the minimum gap spacing and (2) non-vertical sidewalls cause enlarged effective gap spacing and, in particular, significantly reduce the maximum capacitance. The impedance measurement also showed a parallel parasitic resistance R_p of about 800 kΩ to 1 MΩ. This is probably due to partial shortage caused by residuals at the bottom between electrodes or in the spacing between fingers. Fabrication technology is being refined to solve these imperfections.

The parasitic resistance R_p made it impossible to measure the output voltage or power if the device was operated in the dc mode (figure 1). Therefore, an ac mode was used for power measurement, as shown in figure 12. In this mode, an ac current is generated due to the change of C_v and results in an ac output power to the load R_T. Since a series capacitor C_T is used to block the dc path in the device, there is no net power consumption of the test voltage source V_T. In addition, the device does not need to reach the maximum displacement to deliver output power; therefore, the switches in figure 1 are not needed. This mode can be used when the vibration amplitude is lower than the targeted value. Without the external mass, the device in figure 12 was driven with an acceleration of 32.5 m s^{-2} at the resonant frequency $f_0 = 1870$ Hz and a test voltage V_T of 9 V. The displacement was about 9.7 μm. The output voltage V_{out} was measured for various load R_T; the rms output power $P_{out} = V_{out}^2/R_T$ was calculated and shown in figure 13. A maximum output power of 1.2 μW was obtained for a load of $R_T = 5$ MΩ. However, the observed output voltage V_{out} was of the same frequency f_0 as the vibration source while the variation of the capacitance C_v between the comb fingers and its induced current were of $2f_0$. This indicates that the measured power was not due to the variable capacitance C_v between fingers. A possible source of this measured power is the parasitic capacitance C_v' between the movable fingers and the substrate which had a relative motion at f_0. The substrate was connected to the circuit board during the measurement, as shown in figure 12. The circuit in figure 12 was solved

numerically with C_v and C_v' as fitting parameters since they could not be distinguished in the static measurement with the LCR meter. The calculated power with capacitance variation $C_v = 40$–80 pF and $C_v' = 50$–300 pF is shown in figure 13. While the general trend of the measured data agrees well with the calculation, it should be emphasized that the exact values of the fitting parameters and detailed circuit models still need to be confirmed. Such confirmation and experiments with the external mass attached are currently being conducted.

5. Conclusion

The design and analysis of a micro vibration-to-electricity energy converter with integrated mechanical switches is presented. Lateral contact and pull-in mechanisms for mechanical switch design have the advantage of zero charge leakage and synchronous operation to the external vibration. For $V_{in} = 3.6$ V, an input vibration of 2.25 m s^{-2} at 120 Hz, an external mass of 4 g and a maximum proof mass displacement of 25.4 μm, the device is designed to produce a 31 μW output power. Devices were fabricated in SOI wafers. Due to the unexpected parasitic resistance, the device was measured in an ac mode and an output power of 1.2 μW was obtained for a test voltage V_T of 9 V, an input vibration of 32.5 m s^{-2} at a resonant frequency of 1870 Hz, no external mass attached and maximum displacement of 9.7 μm. The device layout and fabrication processes are currently being re-designed in order to solve the problems with parasitics and dimensional inaccuracy. Detailed circuit modeling and ac output power measurement with the external mass attached are also in progress.

Acknowledgments

This project was supported in part by the National Science Council, Taiwan, ROC, under the grant no NSC 95-2221-E-009-343, the Ministry of Economic Affairs, Taiwan, ROC, under the grant no 95-EC-17-A-07-S1-001 and the College of Electrical Engineering, National Chiao Tung University, Taiwan, ROC, under the grant no 96W826-A. The authors are grateful to the National Center for High-Performance Computing, the National Chip Implantation Center and the National Nano Device Laboratories, Taiwan, ROC, for computer time and facilities.

References

[1] Rabaey J M, Ammer M J, da Silva J L Jr, Patel D and Roundy S 2000 PicoRadio supports ad hoc ultra-low power wireless networking *IEEE Comput.* **33** 42–8

[2] Tashiro R, Kabei N, Katayama K, Ishizuka Y, Tsuboi F and Tsuchiya K 2000 Development of an electrostatic generator that harnesses the motion of a living body: use of a resonant phenomenon *JSME Int. J.* C **43** 916–22

[3] Penella M T and Gasulla M 2007 Runtime extension of autonomous sensors using battery-capacitor storage *Proc. Int. Conf. on Sensor Technol. Appl. Sensor Comm. 2007* pp 325–30

[4] Harb J N, LaFollette R M, Selfridge R H and Howell L L 2002 Microbatteries for self-sustained hybrid micropower supplies *J. Power Sources* **104** 46–51

[5] Heinzel A, Hebling C, Muller M, Zedda M and Muller C 2002 Fuel cells for low power applications *J. Power Sources* **105** 250–5

[6] Frechette L G, Lee C, Arslan S and Liu Y C 2003 Design of a microfabricated Rankine cycle steam turbine for power generation *Proc. ASME IMECE 2003 (Washington, DC)* paper no. IMECE-42082

[7] Li H and Lal A 2002 Self-reciprocating radioisotope powered cantilever *J. Appl. Phys.* **92** 1122–7

[8] Amirtharajah R and Chandrakasan A 1998 Self-powered signal processing using vibration-based power generation *IEEE J. Solid-State Circuits* **33** 687–95

[9] Raghunathan V, Kansal A, Hsu J, Friedman J and Srivastava M 2005 Design considerations for solar energy harvesting wireless embedded systems *Proc. 4th Int. Symp. Information Processing in Sensor Networks* pp 457–62

[10] Roundy S, Otis B P, Chee Y-H, Rabaey J M and Wright P 2003 A 1.9 GHz transmit beacon using environmentally scavenged energy *Proc. Int. Symp. on Low Power Electronics and Design*

[11] Castano E, Revuelto E, Martin M C, Garcia-Alonso A and Garcia F J 1997 Metallic thin-film thermocouple for thermoelectric microgenerator *Sensors Actuators* A **60** 65–7

[12] Strasser M, Aigner R, Lauterbach C, Sturm T F, Franosch M and Wachutka G 2004 Micromachined CMOS thermoelectric generators as on-chip power supply *Sensors Actuators* A **114** 362–70

[13] Huesgen T, Woias P and Kockmanna N 2008 Design and fabrication of MEMS thermoelectric generators with high temperature efficiency *Sensors Actuators* A **145–146** 423–9

[14] Starner T 1996 Human-powered wearable computing *IBM Syst. J.* **35** 618–29

[15] Shenck N and Paradiso J 2001 Energy scavenging with shoe-mounted piezoelectrics *IEEE Micro* **21** 30–42

[16] Federspiel C C and Chen J 2003 Air-powered sensor *Proc. IEEE Sensors* pp 22–5

[17] Chen C-T, Islam R A and Priya S 2006 Electric energy generator *IEEE Trans. Ultrason., Ferroelectr. Freq. Control* **53** 656–61

[18] Horowitz S B, Sheplak M, Cattafesta L N and Nishida T 2006 A MEMS acoustic energy harvester *J. Micromech. Microeng.* **16** S174–81

[19] Roundy S, Wright P K and Rabaey J M 2003 *Energy Scavenging for Wireless Sensor Networks with Special Focus on Vibrations* (Dordrecht: Kluwer)

[20] Williams C B and Yates R B 1996 Analysis of a micro-electric generator for microsystems *Sensor Actuators* A **52** 8–11

[21] Shearwood C and Yates R B 1997 Development of an electromagnetic microgenerator *Electron. Lett.* **33** 1883–4

[22] Glynne-Jones P, Tudor M J, Beeby S P and White N M 2004 An electromagnetic, vibration-powered generator for intelligent sensor systems *Sensors Actuators* A **110** 344–9

[23] Beeby S P, Tudor M J, Torah R N, Roberts S, O'Donnell T and Roy S 2007 Experimental comparison of macro and micro scale electromagnetic vibration powered generators *Microsyst. Technol.* **13** 1647–53

[24] Mitcheson P D, Miao P, Stark B H, Yeatman E M, Holmes A S and Green T C 2004 MEMS electrostatic micropower generator for low frequency operation *Sensors Actuators* A **115** 523–9

[25] Meninger S, Mur-Miranda J O, Amirtharajah R, Chandrakasan A and Lang J 1999 Vibration-to-electric conversion *Proc. Int. Symp. on Low Power Electronics and Design* pp 48–53

[26] Yen B C and Lang J H 2006 A variable-capacitance vibration-to-electric energy harvester *IEEE Trans. Circuits Syst.* **53** 288–95
[27] Chiu Y, Kuo C T and Chu Y S 2007 MEMS design and fabrication of an electrostatic vibration-to-electricity energy converter *Microsyst. Technol.* **13** 1663–9
[28] Roundy S, Wright P K and Pister K S J 2002 Micro-electrostatic vibration-to-electricity converters *Proc. ASME IMECE 2002 (New Orleans, LA)* paper no. IMECE-39309
[29] Marzencki M, Ammar Y and Basrour S 2007 Integrated power harvesting system including a MEMS generator and a power management circuit *Sensors Actuators* A **145–146** 363–70
[30] Ottman G K, Hofmann H F and Lesieutre G A 2003 Optimized piezoelectric energy harvesting circuit using step-down converter in discontinuous conduction mode *IEEE Trans. Power Electron.* **18** 696–703
[31] White N M, Glynne-Jones P and Beeby S P 2001 A novel thick-film piezoelectric micro-generator *Smart Mater. Struct.* **10** 850–2
[32] Roundy S, Leland E S, Baker J, Carleton E, Reilly E, Lai E, Otis B, Rabaey J M, Wright P K and Sundararajan V 2005 Improving power output for vibration-based energy scavengers *IEEE Pervasive Comput.* **4** 28–36
[33] Peano F and Tambosso T 2005 Design and optimization of a MEMS electret-based capacitive energy scavenger *J. Microelectromech. Syst.* **14** 429–35
[34] Sterken T, Fiorini P, Baert K, Puers R and Borghs G 2003 An electret-based electrostatic μ-generator *Proc. 12th Int. Conf. on Solid-State Sensors, Actuators and Microsystems (TRANSDUCERS)* pp 1291–4
[35] Kuehne I, Frey A, Marinkovic D, Eckstein G and Seidel H 2008 Power MEMS—a capacitive vibration-to-electrical energy converter with built-in voltage *Sensors Actuators* A **142** 263–9
[36] Miyazaki M, Tanaka H, Ono G, Nagano T, Ohkubo N, Kawahara T and Yano K 2003 Electric-energy generation using variable-capacitive resonator for power-free LSI: efficiency analysis and fundamental experiment *Proc. Int. Symp. on Low Power Electronics and Design* pp 193–8
[37] Mitcheson P D, Green T C and Yeatman E M 2007 Power processing circuits for electromagnetic, electrostatic and piezoelectric inertial energy scavengers *Microsyst. Technol.* **13** 1629–35
[38] Rebeiz G M 2003 *RF MEMS Theory, Design, and Technology* (New York: Wiley) pp 37–8
[39] Chiu Y and Pan J H 2007 Micro knife-edge optical measurement device in a silicon-on-insulator substrate *Opt. Exp.* **15** 6367–73